# Charles University
# Faculty of Science

Study programme: Applied Geology



## Haiquan Sun


**Investigation of the thermo-hydro-mechanical behavior of Czech bentonite used as a model material for planning of high level nuclear waste disposal**

Doctoral thesis


Supervisor: doc. RNDr. David Mašín, Ph.D.



Prague, 2019

*To my parents*

# Declatation of the student

I declear that I have prepared and elaborated this thesis on my own. This thesis neither any of its parts were not used to obtain any other academic degree. All used references and source of information are listed at the end of the thesis.

In Prague, 18 July 2019

Haiquan Sun

# Acknowledgements

At this moment, I would like to thank my supervisor doc. RNDr. David Mašín, Ph.D. for his professional instructions, patience, guidance and encouragement in my doctoral research. Many thanks to Ing. Jan Boháč, CSc., and RNDr. Jan Najser, Ph.D. for their help and suggestions in my laboratory work. I would like to thank my colleagues Jan Jerman, Tomáš Mohyla, Jakub Roháč and Monika Černíková for their help during my study at Charles University.

Finally, I would like to appreciate my parents and my younger sister for their strong support and encouragement.

The work presented in this thesis was supported by Grant 846216 and 1476119 of the Grant Agency of the Charles University. This work receives funding from the Euratom research and training programme 2014-2018 under grant agreement No 745942. Also, financial support by the TACR grant TK01010063 and TK01030031 is greatly appreciated.

# Contents

# List of Figures

# List of Tables

# Symbols and abbreviations

| | |
|---|---|
| B | base cation exchange capacity |
| C | constants |
| C` | constants |
| D | entrance pore diameter |
| d | half of the distance of clay platelets |
| $D_b$ | box counting pore surface fractal dimension |
| DDL | diffuse double layer |
| $D_s$ | pore surface fractal dimension by Menger fractal model |
| $D_w$ | dielectric constant of bulk fluid |
| $D_z$ | thermal fractal dimension |
| e | void ratio |
| e` | elementary electric charge |
| ESEM | environmental scanning electron microscope |
| $\varepsilon_0$ | permittivity of vacuum |
| G | specific gravity |
| i | i-th intrusion step |
| k | Boltzmann's constant |
| K | diffuse double layer parameter |
| MIP | mercury intrusion porosimetry |
| $n_0$ | ionic concentration of the bulk fluid |
| P | intrusion pressure |
| p | swelling pressure |
| $Q_n$ | a function of pore radius and pore volume |
| r | pore radius |
| S | specific surface area |
| T | absolute temperature in Kelvin |
| u | nondimensional midplane potential |
| v | weighted average of valency |
| $V_{max}$ | total volume intruded at the maximum intrusion pressure |

| | |
|---|---|
| $V_p$ | cumulative volume at pressure of p |
| $W_n$ | accumulated surface energy |
| WRC | water retention curves |
| y | nondimensional potential at a distance x from the clay surface |
| z | nondimensional potential function at the surface (x = 0) |
| $\gamma_d$ | dry density |
| $\gamma_w$ | density of water |
| $\zeta$ | distance function |
| $\theta_{nw}$ | contact angle between the mercury and soil surface |
| $\rho_d$ | initial dry density |
| $\sigma_{cs}$ | swelling pressure determined by saturated oedometer test |
| $\sigma_{cv}$ | swelling pressure at constant volume |
| $\sigma_{Hg}$ | surface tension of mercury |
| $\sigma_v$` | constant load |

# List of publictions

## Journal articles

1) **Sun, H**., Mašín, D., Najser, J., Neděla, V., & Navrátilová, E. (2019). Bentonite microstructure and saturation evolution in wetting–drying cycles evaluated using ESEM, MIP and WRC measurements. Géotechnique, 69(8), pp. 713-726, doi: doi.org/10.1680/jgeot.17.P.253

2) **Sun, H** (2018). A new method to predict swelling pressure of compacted bentonites based on diffuse double layer theory. Geomechanics and Engineering, 16(1), 71–83. https://doi.org/10.12989/GAE.2018.16.1.071

3) **Sun, H**., Mašín, D. Najser, J., Neděla, V., & Navrátilová, E. (2019), Fractal characteristics of pore structure of compacted bentonite studied by ESEM and MIP methods, Acta Geotechnica (Accepted)

## International Conference proceedings

1) **Sun, H**., Mašín, D., & Najser, J. (2018, May). Thermal Water Retention Characteristics of Compacted Bentonite. In GeoShanghai International Conference (pp. 71-78). Springer, Singapore.

2) **Sun, H**., Mašín, D., & Najser, J.(2018). Investigation of the mechanical behavior of compacted bentonite. The 7th International Conference on Unsaturated Soils Conference, Hong Kong

3) **Sun, H**., Mašín, D., & Najser, J. (2018). Experimental Study on Highly Compacted Bentonite Aggregates Subjected to Wetting and Drying. In Proceedings of China-Europe Conference on Geotechnical Engineering (pp. 1632-1635). Springer, Cham.

4) **Sun, H**., Mašín, D., & Boháč, J. (2017). Experimental characterization of retention properties and microstructure of the Czech bentonite B75. In *Proceedings of the 19th International Conference on Soil Mechanics and Geotechnical Engineering, Seoul* (pp. 1249-1252).

5) **Sun, H**. (2017, July). Prediction of Swelling Pressure of Compacted Bentonite with Respect to Void Ratio Based on Diffuse Double Layer Theory. In International Congress and Exhibition" Sustainable Civil Infrastructures: Innovative Infrastructure Geotechnology" (pp. 89-104). Springer, Cham.

# Abstract

The work involved in the thesis is mainly focused on the Czech bentonite which is originally from Cerny vrch deposit (north western region of the Czech Republic). The compacted bentonites are prepared from the industry provided bentonite powder with an initial water content around 10%. Dry densities from 1.27 to 2 g/cm$^3$ were used for laboratory testing, specifically 1.27, 1.60 and 1.90 g/cm$^3$ were used for water retention measurements, microstructures and fractal pore analysis. Dry densities of 1.25 to 1.95 g/cm$^3$ were used for mechanical tests such as one dimensional swelling strain and oedometer load-unload tests. The vapor equilibrium method was used to impose the suction on samples ranging from 3.29 MPa to 286.7 MPa. Mercury intrusion porosimetry (MIP) and environmental scanning electron microscope (ESEM) were utilized for the microstructure analysis. The water retention measurements were performed at 20, 40, 60 and 80 °C respectively, results show that the increasing of temperature can decrease the water retention capacity. The influence of compaction and suction on microstructure was compared and studied. MIP tests were performed on the samples which were equilibrated at suction of 3.29, 38 and 286.7 MPa on wetting path of both low and high dry densities. The samples equilibrated at suction of 286.7 MPa on wetting path were firstly observed in ESEM chamber with different magnification, then followed by wetting and drying path performed in the chamber with increasing and decreasing relative humidity. The changes in aggregates and macropores were recorded. The pore families (macropores and micropores) recognized by the MIP results were consistent with the ESEM observation. Moreover, the influence of dry density and suction on the microstructure was studied by fractal analysis with different methods. Fractal analysis confirmed the pore families definition by MIP pore size distribution curve. The mechanical study of compacted bentonite showed a unique relationship between (aggregate) dry density and effective stress. The proposed equations for predicting swelling pressure were developed based on the diffuse double layer (DDL) theory, which was proved to be applicable in both sodium and calcium bentonites. The prediction of swelling pressure of Czech bentonite was presented and discussed.

# Abstrakt

Práce se se zaměřují především na český bentonitu, který je původem z lokality Černý vrch (severozápadní oblast České republiky). Bentonit se připravuje průmyslově hutněním, přičemž bentonitový prášek má počáteční obsah vody asi 10%. Hustoty v suchém stavu jsou od 1,27 do 2 g / $cm^3$, přičemž pro laboratorní testy byly konkrétně použity hustoty 1,27, 1,60 a 1,90 g / $cm^3$. Tyto hustoty byly použity pro měření retenčních čar, mikrostruktury a fraktální analýzy pórů. Suchá objemová hmotnost od 1,25 do 1,95 g / $cm^3$ byla použita pro mechanické zkoušky, jako jednorozměrné bobtnání a edometrické zatížení a odlehčení. Metoda rovnováhy par byla použita k předepsání sání v rozmezí od 3,29 MPa do 286,7 MPa. Pro analýzu mikrostruktury byla využita rtuťová intrusní porozimetrie (MIP) a environmentální rastrovací elektronový mikroskop (ESEM). Měření retenčních čar bylo prováděno při 20, 40, 60 a 80° C. Výsledky ukazují, že zvýšení teploty může snížit schopnost zadržování vody. Byl také porovnáván a studován vliv zhutnění a bobtnání na mikrostrukturu. MIP testy byly prováděny na vzorcích, které byly ekvilibrovány při sáních 3, 29 , 38 a 286,7 MPa na smáčecí dráze jak za nízkých, tak za vysokých suchých objemových hmotnostech. Vzorky připravené při sáních 286,7 MPa na zvlhčovací větvy byly nejprve pozorované v ESEM komoře s různým zvětšením, pak následovala zvlhčovací z vysušovací cesta v komoře se zvyšováním a snižováním relativní vlhkosti. Snímkování pomohlo identifikovat póry dvou rodin (makropóry a mikropóry). Dále byl studován vliv suché hustoty a sání na mikrostrukturu pomocí fraktální analýzy různými metodami. Fraktální analýza potvrdila definici pórových rodin pomocí křivky distribuce velikosti pórů MIP. Mechanické studium zhutněného bentonitu ukázalo jedinečný vztah mezi suchou hustoty a bobtnacím napětím. Navrhované rovnice pro predikci bobtnajícího tlaku byly vyvinuty na základě teorie difúzní dvojité vrstvy (DDL), která se ukázala být použitelná jak na sodném, tak na vápenatém bentonitu. Dále byla prezentována a diskutována predikce bobtnacího tlaku na českém bentonitu.

# 1. Introduction

## 1.1 Research background

With the increasing utilization of nuclear energy, the wasted high level spent nuclear fuel must be properly and safely stored. The most appropriate way to handle these high level nuclear waste is the deep geological disposal, which is usually excavated in depths of 400 - 500 meters in the natural rock formations. The principle of deep geological disposal is to isolate the waste from the human being biosphere environment for more than 1 million years until its radioavtivity decayes to harmless levels. Considering the safety of the deep geological disposal, barriers are usually used to keep the system independent. Bentonite material was popularly chosen as the barriers, thanks to its low permeability, high adsorption potention and high swelling pressure. Bentonite is a clay of high montmorillonite content. The compacted bentonite is used as engineered barrier material between canister and surrounding rocks, while the bentonite pellets is planned to be used as backfill materials to fill the disposal tunnels. The initially unsaturated compacted bentonite near the rock will be hydrated by the underground water, while the bentonite near the canister will be heated by the radioactivity generated by the spent fuel. When the bentonite adsorbs water, the swelling pressure will be generated. The swelling properties are related to the type and the initial state of bentonite. Thus, understanding the thermo-hydro-mechanical behavior of bentonite is necessary for the properly choosing of barrier materials and safety operation of the nuclear waste disposal.

Over the past decades, bentonite has been an extensively studied material. It is now well accepted that compacted bentonite has a structure with two distinct pore systems, denoted as a double structure (Gens & Alonso, 1992; Alonso et al., 1999, 2010). The double structure plays an important role in the thermo-hydro-mechanical behavior of compacted bentonite and it is explicitly considered in many bentonite constitutive models. The microstructure is investigated using mercury intrusion porosimetry (MIP) and an environmental scanning electron microscopy (ESEM) method, which is supplemented by water retention measurements.

The water retention properties of compacted clay/bentonite have been related to its microstructure presented by various authors. Villar (2007) observed that the water retention curve (WRC) was not dependent on relative density for suctions higher than 10 MPa. Similar observations have been made by Romero & Vaunat (2000) and Romero et al. (2011), who

adopted a double-structure framework to interpret water retention behavior. A similar approach was chosen by Dieudonne et al. (2017), who considered adsorbed water in the micropores and capillary water in the macropores separately.

Typically most of models consider the double structure as modeling approach. However, in several recent studies, it has been suggested that the consideration of two pore families may be an oversimplification of the complex bentonite structure. For example, Wang et al. (2014) identified four major pores by MIP tests, Přikryl and Weishauptová (2010) investigated the hierarchical porosity of the Czech bentonite from Rokle deposit (similar to the one used in this study). Four pore size categories were identified by adsorption isotherms and MIP tests, Monroy et al. (2012) summarized three pores families for compacted London Clay. The influence of compaction and suction on the pore size distribution of compacted clay were investigated by Hattab et al., 2013 and Seiphoori et al.,2014.

The environmental scanning electron microscopy (ESEM) observation is usually combined with MIP to interpret the microstructure of bentonite. This technique is more advanced than the traditional SEM. The ESEM can let us directly observe samples under different relative humidity conditions. To effectively and quantitatively utilize the MIP and ESEM data, the fractal dimension is a good choice to study the microstructure of compacted bentonite. Fractal dimension has been proven to be an efficient tool to describe and study the pore irregularity and surface roughness of different porous materials, such as the heterogeneities of pore spaces in sedimentary rocks (Wong and Howard, 1986; Flavio et al.,1998), the fractal characteristic of micropores on the fracture surface of sandstone (Hansen and Skjeltorp, 1998; Turcotte, 2002), and the methane and gas adsorption of coals (Mahamud et al., 2013; Liu and Nie, 2016). The fractal dimension of clay related to its structure has also been studied by many researchers (Vallejo, 1996; Hyslip and Vallejo, 1997; Romero, 1999; Romero and Simms, 2008; Farulla and Jommi, 2003; Cui et al., 2016).

The microstructure of bentonite mainly contains bentonite aggregates (clay plates) and pores, in which the pores existing between aggregates are named macropores, whereas the pores within aggregates are named micropores. The basic unit to constitute clay is the unit layer which consists of an aluminum octahedral sheet sandwiched between two silica tetrahedral sheets. The basic unit layers and the attached cations have significant influence on the water retention properties, thermal and mechanical behavior. The diffuse double layer (DDL) theory considered the clay-water-electrolyte interaction, which is an effective tool to study the swelling pressure. The basic form of DDL theory was proposed by Gouy-Chapman (Gouy 1910, Chapman 1913).

According to DDL theory, the interaction forces between double layers depend on the midplane potential and ion concentration at midplane and its value equals to the osmotic pressure in that plane (Bolt 1956). It is shown that the DDL theory can predict well swelling pressure for a dry densities lower than 1.55 g/cm$^3$ (Schanz and Tripathy, 2009). Komine and Ogata (1996) pointed out that the DDL can predict adequately the swelling characteristics of compacted bentonite when the swelling pressure is less than about 3 MPa and the type is sodium bentonite (Kunigel). Tripathy et al., (2004) summarize three equations based on DDL by considering the weighted average valency of cations, while it didn't work well on Bavaria bentonite in the high dry density range (Schanz and Tripathy, 2009). Thus, the improvement of the basic DDL is necessary.

## 1.2 Organization of the thesis

The thesis includes seven chapters. Chapter 1 presents the research background and organization of the thesis. Chapter 2 gives a short introduction of the aim of the thesis. Chapter 3 presents the materials and methods used in the thesis. Chapter 4 presents all the tests results and discussions. More detailed, in section 4.1, the water retention properties under 20 - 80 °C are presented (parts of the results were published in Géotechnique journal and Geoshanghai 2018 conference proceedings). In section 4.2, the microstructure of the bentonite under different compaction and suction are presented and discussed (these results were published in Géotechnique journal, Acta Geotechnica journal and presented in 19th ICSMGE and IS Atlanta 2018 conference). In section 4.3, the mechanical behavior is presented (parts of the results were published in Geomechanics and Engineering journal and presented in UNSAT2018 and GeoMEast 2017 conference). The conclusions is summarized in Chapter 5. Chapter 6 listes all the references used in the thesis. Finally, the three impact factor journal articles are attached in Chapter 7.

# 2. Aim of the thesis

The work involved in this thesis is targeting at better understanding of the behavior of the Czech bentonite at various conditions. The aim of this thesis is to study the thermo-hydro-mechanical properties of Czech bentonite by laboratory tests and modeling, which are key in dealing with the backfill materials or the engineered barrier systems utilized in planned high level nuclear waste disposal galleries. The water retention properties, microstructure characteristics and mechanical behavior of the Czech bentonite are presented in this thesis. The results obtained in the thesis can further be used for bentonite material evaluation and also as input data to simulate the behavior of bentonite performed in mock-up tests by modeling.

# 3. Materials and methods

## 3.1 Materials

The thesis mainly focus on the Czech bentonite extracted from the Cerny vrch deposit (north-western region of the Czech Republic). It is commercially supplied in the form of powder, but B75 was specially treated by slight vitrification only. The initial water content of the bentonite powder was around 10%. The montmorillonite content was about 60%. Table 1 lists its physical parameters. The plastic limit, liquid limit and specific gravity of the solid are 65%, 229% and 2.87, respectively. The cation exchange capacity is shown in Table 2.

*Table 1. Montmorillonite content and physical properties of bentonite B75 (Stastka and Smutek, 2015)*

| Property | Description |
|---|---|
| Montmorillonite (%) | 60 |
| Liquid limit (%) | 229 |
| Plastic limit (%) | 65 |
| Plasticity index Ip | 164 |
| Particle density $\rho_s$ (g/cm$^3$) | 2.87 |

*Table 2. Cation exchange capacity of bentonite B75 (Sun et al., 2017)*

| Cation | meq/100g |
|---|---|
| $Ca^{2+}$ | 36.92 |
| $Na^{+}$ | 65.75 |
| $K^{+}$ | 3.03 |
| $Mg^{2+}$ | 26.84 |
| $H^{+}$ | <0.5 |

## 3.2 Methods

### 3.2.1 Vapor equilibrium method

The vapor equilibrium method (Delage et al. 1998) was applied to control the total suction. Relative humidity in the closed desiccator was controlled by different saturated salt solutions, the values of which were dependent on temperature. In this thesis, eight different salt solutions were used and the value of relative humidity as shown in Table 3. The total suction can be calculated by the Kelvin equation by knowing the value of relative humidity. The temperature was imposed at 20, 40, 60 and 80 °C respectively. The 20 °C tests were performed in the air condition room with constant temperature. Other higher temperatures tests were done in a temperature controlled box, in which the desiccators were placed in. The suction varied from 3.29 MPa to 286.7 MPa (20 °C). The compacted samples (0.8-5 g) were placed in the glass dishes which were placed on a plate with holes above the saturated solutions (Figure 1). The weight of the samples was checked periodically. This method was quite simple but time consuming, usually it took more than 2-3 months to reach the equilibrium state (Sun et al., 2018a).

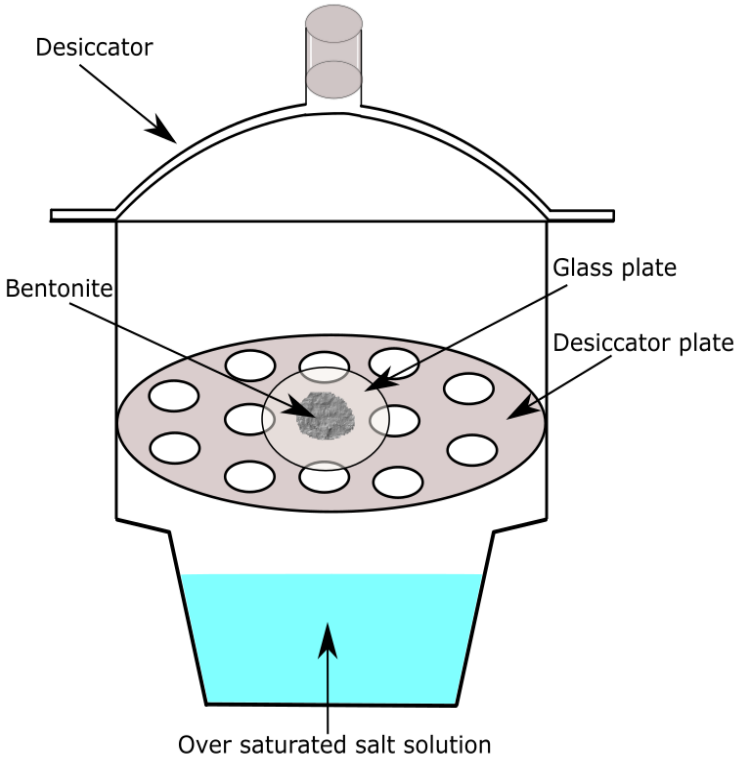


*Figure 1. Vapor equilibrium methods*

*Table 3. Relative humidity and suction imposed by saturated saline solution for vapor equilibrium methods (adopted from Haynes (2014), OIML(1996), Tang and Cui (2005)).*

| Chemical Solution | Relative humidity (%) | | | |
|---|---|---|---|---|
| Temperature | 20 °C | 40 °C | 60 °C | 80 °C |
| $LiCl \cdot H_2O$ | 11.31 | 11.21 | 10.95 | 10.51 |
| $CH_3COOK$ | 23.11 | - | - | - |
| $MgCl_2 \cdot 6H_2O$ | 33.07 | 31.6 | 29.26 | 26.05 |
| $K_2CO_3$ | 43.16 | - | - | - |
| NaBr | 59.1 | 53.2 | 49.7 | 51.4 |
| NaCl | 75.47 | 74.68 | 74.5 | 76.29 |
| KCl | 85.1 | 82.3 | 80.3 | 78.9 |
| $K_2SO_4$ | 97.2 | 96.5 | 96.2 | 95.5 |

### 3.2.2 Mercury intrusion porosimetry

Mercury intrusion porosimetry (MIP) is based on the capillary law governing non-wetting liquid penetration into small pores. The pore entrance diameter (D) can be determined from the applied mercury pressure (P) by assuming that the cylindrical pores existed in soil according to Washburn equation (Juang and Holtz, 1986):

$$D = -(4\sigma_{Hg} cos\theta_{nw})/P \quad (1)$$

Where D is the entrance pore diameter, $\sigma_{Hg}$ is the surface tension of mercury, $\theta_{nw}$ is the contact angle between the mercury and soil surface and P is the intrusion pressure. In this study, $\theta_{nw}$ =130° and $\sigma_{Hg}$ =0.484 N/m at 25 °C were considered in pore diameter calculation.

The MIP tests were performed at the Department of Inorganic Technology at the University of Chemistry and Technology Prague (Apparatus Autopore IV, Micromeritics). The measurement was done in two regimes, one was the low pressure regime from 0.01 MPa to 0.2 MPa (corresponding to the pore radius between 100 μm and 3 μm); another one was the high pressure regime from 0.2 MPa to 400 MPa (corresponding the pore radius between 3μm to 1.5 nm). MIP tests were conducted on freeze dried samples, which can keep its original structure. In freeze drying methods, the samples were firstly immersed into the liquid nitrogen to quickly freeze to preserve its original structure, then the frozen samples were placed under deep vacuum. Finally, the samples went through sublimation in the vacuumed chamber of a freeze dryer.

### 3.2.3 Environmental SEM observations

The environmental scanning electron microscope (ESEM) is widely used for the observations of micro-fabric. And the ESEM has advantages with respect to traditional SEM, the former can be used for observation under different relative humidity, while the latter is only suitable for completely dry samples which only can be observed at the atmospheric pressure and laboratory temperature. Combination of optical and electron microscopy is effective to study macro- to micro-structural changes of clay, soils or other geological materials caused by swelling and shrinking.

The Environmental Scanning Electron Microscopy (ESEM) tests have been performed using QUANTA 650 FEG scanning electron microscope at the Institute of Scientific Instruments of the Czech Academy of Sciences, Brno, Czech Republic. The samples were placed in a special conical holder and cooled by a Peltier stage. This holder allowed minimizing sample shift in conditions of very high relative humidity as well as better cooling which was necessary for sample stabilization and repeatability of observation. Conditions of observation were kept constant throughout the experiment. The compacted bentonite samples were observed at different magnifications (from 800 to 50000 times) at different states. Especially, the bentonite samples with different initial dry densities were observed following wetting and drying path at the magnification of 2500 times. The water vapor pressure of 93 Pa (relative humidity of 10%) was determined as an optimal initial state for the experiment. Then the vapor pressure was gradually increased up to 850 Pa (relative humidity 97%). After the maximum value of the relative humidity was reached, the relative humidity was gradually decreased again down to 10%. The microphotographs were taken at each stage. The time interval between vapor pressure changes was 15 minutes. The test conditions are summarized in Table 4.

*Table 4. Water vapour pressure, temperature, relative humidity and total suction adopted in ESEM measurements*

| Temperature 5 °C | | |
|---|---|---|
| Relative humidity (%) | Water vapour pressure (Pa) | Total suction (MPa) |
| 10 | 93 | 290.75 |
| 30 | 266 | 152.03 |
| 50 | 439 | 87.52 |
| 60 | 519 | 64.50 |
| 74 | 649 | 38.02 |
| 80 | 692 | 28.18 |
| 90 | 785 | 13.30 |
| 97 | 850 | 3.85 |
| 90 | 785 | 13.30 |
| 80 | 692 | 28.18 |
| 74 | 649 | 38.02 |
| 60 | 519 | 64.50 |
| 50 | 439 | 87.52 |
| 30 | 266 | 152.03 |
| 10 | 93 | 290.75 |

### 3.2.4 Oedometer tests

The conventional oedometer apparatus was used for measuring the swelling deformation of Czech bentonite B75. The compacted bentonite was tested in the standard fixed stainless-steel ring, 50 mm inside diameter and 20 mm height. Silicone grease was applied to the inner wall of the stainless-steel ring to reduce friction between the specimen and the wall. The filter papers were placed between the specimen and porous stones. Considering the porous stone placement

and the swelling deformation, the original samples were prepared with the height of 8-10 mm. Once the compacted bentonite was introduced in the stainless-steel ring, the prescribed vertical stress was applied. Then the specimen was infiltrated by distilled water. The vertical deformation and time were recorded. For saturated oedometer test, the loading and unloading test continued after the swelling deformation test. Eventually, the water content of the specimen was measured. The ASTM D2435/D2435M standard recommends the correction for oedometer apparatus compressibility. The deflection of the apparatus was measured by substituting a smooth hard steel disk for the soil specimen before the experiment for all the test conditions.

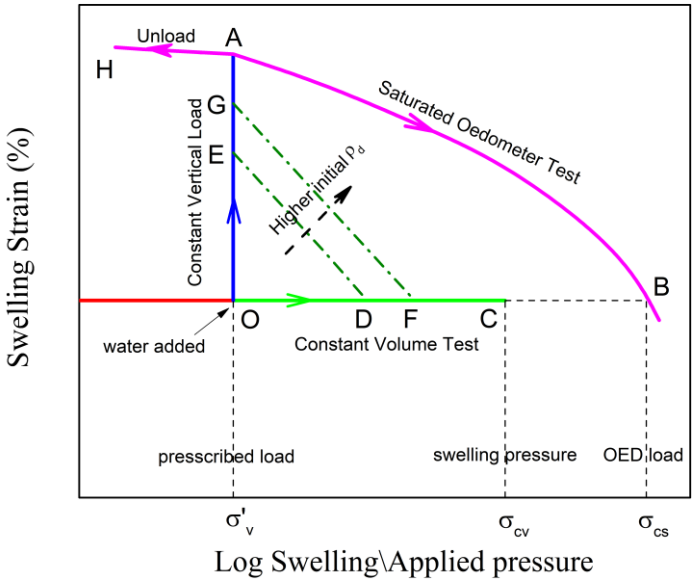


*Figure 2. Effective stress paths of various experimental methods used*

Figure 2 showed the experimental methods used in the mechanical tests. The "saturated oedometer test" method, was also known as "swell-consolidation" method, in which the sample was initially subjected to a prescribed vertical load in the oedometer cell and infiltration under the applied load. The vertical swelling strain occurred due to the hydration and decreasing suction (i.e. path OA). It was obvious that point A represents the maximum swelling strain under constant load $\sigma_v$`. When the swelling process has finished, the vertical stress was gradually increased (path AB). The stress required to bring the volume of the specimen back to its initial value (represented by $\sigma_{cs}$ in Figure 2) was defined as the swelling pressure by Basma et al. (1995). The swelling pressure, $\sigma_{cs}$, measured by the "saturated oedometer test" was higher than the swelling pressure, $\sigma_{cv}$, determined by the constant volume test (Chen, 1988). It may be explained by crystalline expansion due to hydration of absorbed cations on the soil particles and osmotic expansion, in which the soil was probably developing a double diffuse layer.

Generally, it should be easier to prevent water molecules from entering into the soil lattice than to force the water out once it has entered into the soil (Nelson et al., 2015).

## 3.3 Test programme

All the tests programmes including water retention curves (WRC), mercury intrusion porosimetry (MIP), environmental scanning electron microscopy (ESEM) and mechanical tests were presented. Table 5 showed test procedures and initial states of samples in the experiments. The compacted samples were split into two parts. One part was directly equilibrated in the desiccator under controlled suction from 3.29 MPa to 286.7 MPa. The other part was first oven dried. The samples were then either directly equilibrated in a desiccator at various suctions for the wetting path or equilibrated at suction of 3.29 MPa and then moved to the higher suction desiccator for WRC measurements along drying paths. Both the following samples, namely, samples directly equilibrated at the suctions of 3.29, 38 and 286.7 MPa and samples initially oven dried and then equilibrated at the same suction levels – were used for MIP tests. The samples initially oven dried and then equilibrated at 286.7 MPa were used in ESEM observations with changing relative humidity. The mechanical tests programme included swelling at constant vertical load tests with different initial dry density to study the swelling strain behavior. Especially, three different initial dry densities of 1.25, 1.80 and 1.95 g/cm$^3$ were used to explore the influence of vertical stress and initial dry density on swelling strain. Each test required at least two weeks to reach the equilibrium. One saturated oedometer test with an initial dry density of 1.25 g/cm$^3$ and unloading tests with dry densities of 1.80 g/cm$^3$ and 1.95 g/cm$^3$ were conducted. The swelling pressure predicted by the newly developed equations based on diffuse double layer (DDL) theory (Sun 2018) was used to calculate the swelling pressure of Czech bentonite, results were compared with the experimental data (Hausmannova and Vasicek 2014).

3.3 Test programme

*Table 5. Test programme*

| Initial $\rho_d$ | Initial $W_C$ | Initial Suction | Sample state | Suction paths (MPa) |
|---|---|---|---|---|
| 1.27 g/cm$^3$ | 10% | 48.57 MPa | Oven dried | WRC: 286.7→3.29 MPa<br>ESEM: 290.75→3.85→290.75 MPa<br>MIP : 286.7, 38.00, 3.29 MPa |
| | | | Directly equilibrated | MIP : 286.7, 38.00, 3.29 MPa |
| | | | Equilibrated at suction of 3.29MPa | WRC: 286.7→3.29 MPa |
| 1.6 g/cm$^3$ | 10% | 46.65 MPa | Oven dried | WRC: 286.7→3.29 MPa |
| | | | Equilibrated at suction of 3.29MPa | WRC: 286.7→3.29 MPa |
| 1.9 g/cm$^3$ | 10% | 49.29 MPa | Oven dried | WRC: 286.7→3.29 MPa<br>ESEM: 290.75→3.85→290.75 MPa<br>MIP: 286.7, 38.00, 3.29 MPa |
| | | | Directly equilibrated | MIP : 286.7, 38.00, 3.29 MPa |
| | | | Equilibrated at suction of 3.29 MPa | WRC: 286.7→3.29 MPa |

# 4. Results and discussions

This chapter presents all the obtained results which include the water retention properties under low and high temperatures, the microstructure characteristics and the mechanical behavior of compacted bentonite. Each of the main results and findings was introduced in the following sections.

## 4.1 Water retention properties

In this section, the water retention curves of the compacted bentonite at various temperatures are presented. The results presented in subsection 4.1.1 were published in Géotechnique journal (e.g., Sun et al., 2018a) and parts of the results presented in 4.1.2 were published in Geoshanghai 2018 conference proceedings (e.g., Sun et al., 2018b).

### 4.1.1 Water retention curves at room temperature

Figure 3(a) shows the WRCs of samples at three initial dry densities (wetting and drying paths). The wetting path was performed on the samples which were firstly oven dried then moved to each desiccator for wetting path. The prepared samples were firstly equilibrated in low suction desiccator, then distributed to other higher suction desiccators for drying path. It is clear that the initial dry density had only little influence on water content. With the assumption that most water is concentrated in the micropores at high suctions, these results suggest that micropores are only little influenced by the compaction pressures, as if their volume was to be affected, their water retention capacity (which is known to be porosity dependent) would also change. Contrarily, quite a remarkable effect of the initial dry density was found on the degree of saturation (Figure 3(d) and 3(e)) through its effect on the void ratio (Figure 3(b) and 3(c)). Although the void ratio measurements using the wax immersion method were subject to an error (indicated as shaded areas in Figure 3(b) – 3(e)), the measurements consistently show an increase in the global degree of saturation with increasing dry density.

4.1 Water retention properties

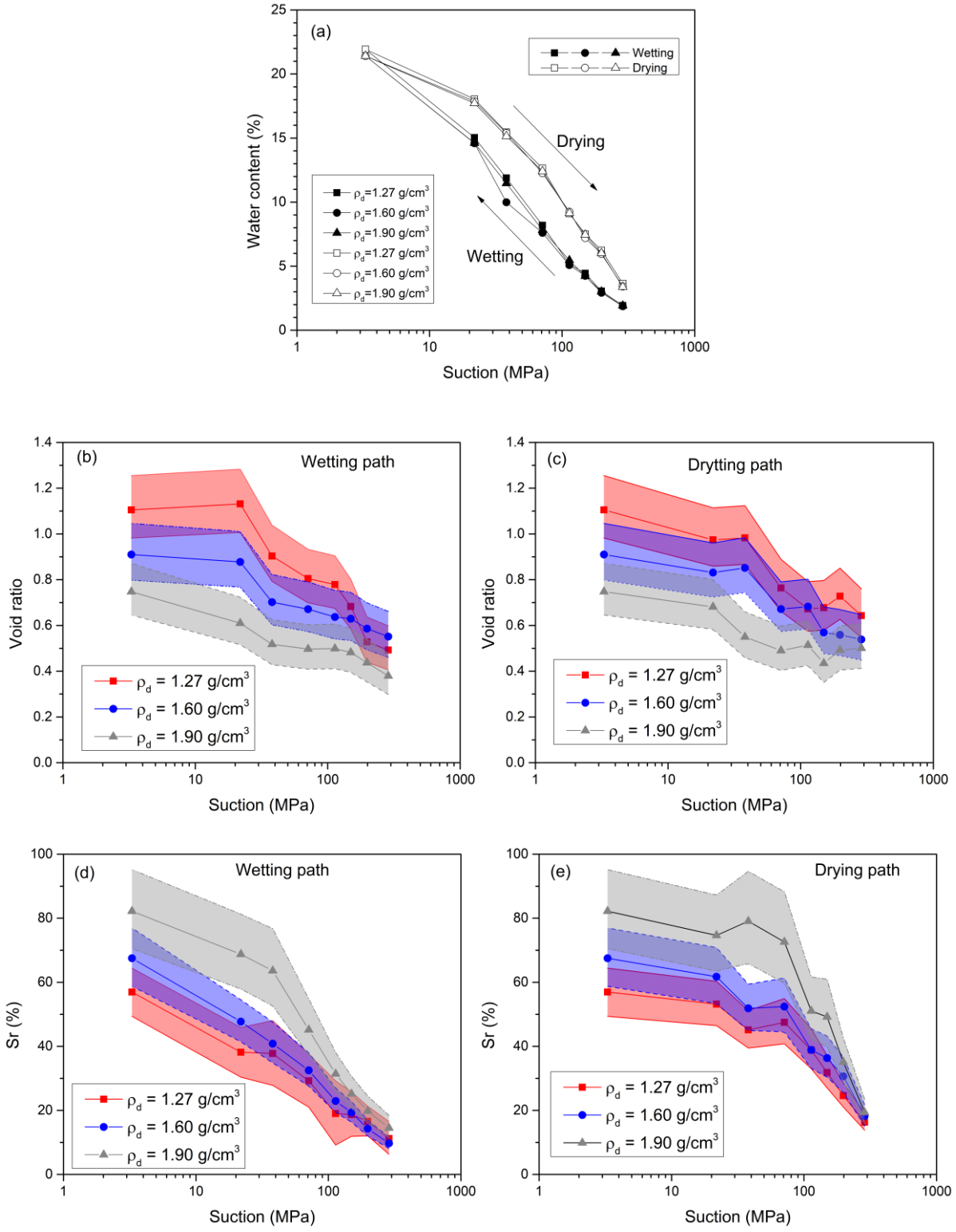


*Figure 3. Water content, void ratio and degree of saturation with respect to suction for water retention curve measurements along wetting and drying path at three different initial dry densities (Sun et al., 2018a).*

### 4.1.2 Water retention curves at high temperature

The water retention curves of three dry densities of 1.27, 1.60 and 1.90 g/cm$^3$ at 20 °C, 40 °C, 60 °C, 80 °C are shown in Figure 4 (a-f) respectively. It can be seen that the water content decreases with increasing temperature for the same initial dry density. This trend was more obvious at low suctions. Comparison of wetting and drying paths showed that wetting curves at high suctions (above 100 MPa) exhibit almost no temperature dependence for all dry densities. The effect of temperature was generally more clear in drying paths. The decrease of water retention capacity with increasing temperature was influenced by the water surface tension, the liquid-gas interfacial tension or contact angle between water and soil. The increased temperature can also drive volumetric changes of the aggregates. These volumetric changes can include both expansion and contraction, depending on initial dry density and applied suction (Villar and Lloret, 2004). These structural changes were associated with the transfer of the intra-aggregate water into inter-aggregate pores, which would explain the lower water retention capacity at a higher temperature at certain suction (Villar and Lloret, 2004). The presented results of Czech bentonite B75 were consistent with this theory and confirmed that the temperature has an important influence on the water retention capacity.

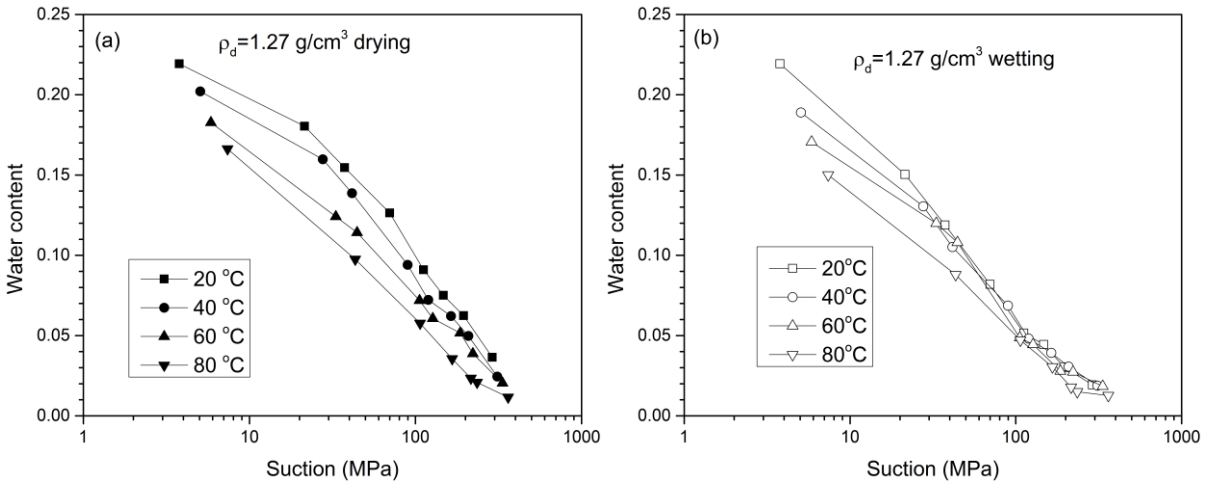

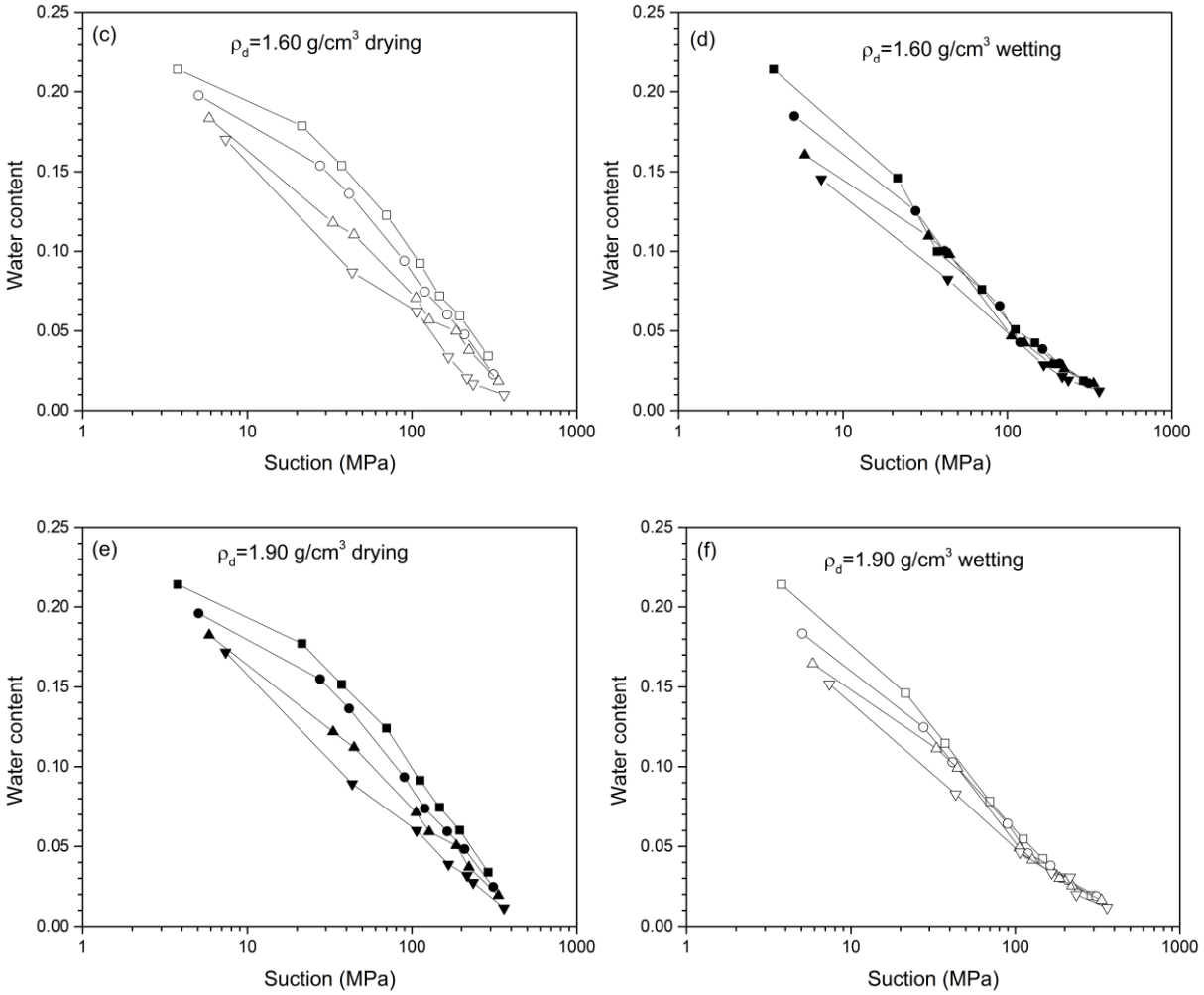


*Figure 4. Water retention curves at various temperatures for dry density of 1.27 g/cm$^3$ ((a) - drying path; (b) – wetting path), 1.6 g/cm$^3$ ((c) - drying path, (d) – wetting path) and 1.9 g/cm$^3$ ((e) - drying path, (f) – wetting path).*

## 4.2 Microstructure evaluation

In this section, the microstructure of the compacted Czech bentonite under different suctions (relative humidity) was studied by MIP and ESEM tests. The pore size distribution curves of different initial dry density with different suction were presented in 4.2.1. Apart from the pores which can not be detected by MIP, two pore families were recognized, namely macropores and micropores. The transition pore size between macropores and micropores was found suction dependent. In subsection 4.2.2, the different pore sizes can be observed by the ESEM microphotos under different magnifications. The changing of volume of aggregates and the pore size were recorded by ESEM microphotos upon drying and wetting path. Results show that the macropores remained dry at most suction levels and the aggregate volume increased sharply at

low suction range (high relative humidity). The results presented in subsection 4.2.1 and 4.2.2 were published in Géotechnique journal (Sun et al., 2018) and presented in ICSMGE 2017 conference (Sun et al., 2017) in Seoul. Another approach to investigate the pore structures was fractal analysis. Pore surface fractal dimension ($D_s$) and thermal fractal dimension ($D_z$) were calculated based on the MIP data, box counting surface fractal dimension ($D_b$) was calculated based on ESEM images. The macropores and micropores were defined based on the fractal analysis, which was consistent with the pore size distribution curves. The influence of drying methods, observation scale, compaction, suction, etc were discussed in subsection 4.2.3. The results were published in Acta Geotechnica journal (e.g., Sun et al., 2019) and presented in IS Atlanta 2018 conference.

### 4.2.1 Mercury intrusion porosimetry

Figure 5 shows the MIP results of low (1.27 g/cm$^3$) and high (1.90 g/cm$^3$) density samples at different suction levels. It clearly identifies the effect of suction on pore size density curves. The MIP data allows us to identify the effects of suction and compaction level on the individual pore sizes. We can distinguish three pore size domains:

1) “Nanopores”: smaller than 3nm. These pores can be attributed to the inter-layer of clay sheets. They can’t be detected by the MIP technique and thus they are not indicated in Figure 5.

2) “Micropores”: between 3nm and micro-macro transition pore radius, which is found to be suction dependent. In this paper, the upper limits of 0.07 μm, 0.15 μm, and 0.3 μm were found to correspond to the suction of 286.7 MPa, 38MPa and 3.29 MPa respectively based on high density samples (in low density samples, the transition pore radius is not clear due to the dominant effect of macropores). It follows from Figure 5 that the largest micropores are influenced by suction and micropores are, in general, unaffected by compaction level.

3) “Macropores”, which are larger than the micro-macro transition pore radius. Macropores up to approximately 2 μm are significantly influenced by compaction level and they are not significantly affected by suction. Contrary, macropores larger than approx. 2 μm are affected both by suction and by compaction.

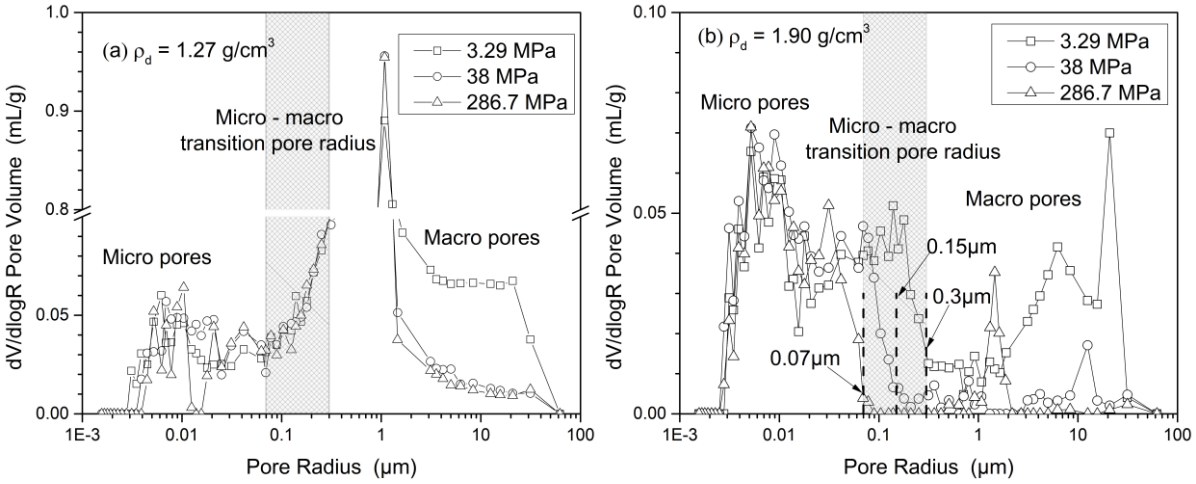


*Figure 5. Pore size distribution curves – the effect of suction and indication of micro-macro transition pore radius: (a) $\rho_d$ = 1.27 g/cm$^3$, (b) $\rho_d$ = 1.90 g/cm$^3$ (Sun et al., 2018a).*

### 4.2.2 Environmental SEM observations

The micrographs of compacted bentonite equilibrated at the suction of 286.7 MPa with an initial dry density of 1.27 g/cm$^3$ is presented in Figure 6. The arrangement of the aggregates may clearly be seen, along with different pore families. The aggregates are clearly visible at lower magnification (Complete photo and Zoom 1), Zoom 2 and Zoom 3 then showed details of the microstructure. The micrographs of compacted bentonite upon subject to wetting and drying in the ESEM chamber were presented in Figure 7 for dry density of 1.27 g/cm$^3$ and in Figure 8 for dry density of 1.90 g/cm$^3$. The relative position of the aggregates (indicated by double arrow), the volume of aggregates and the distance between the aggregates have changed at wetting and drying paths. These photos were qualitatively consistent with MIP observations: macropores and distinct aggregates were visible at low dry density sample, only aggregates with fine bentonite matrix, without clear macroporosity, was visible at high dry density samples. It was also clear that macropores remained dry at most suction levels, apart of lowest suction at high dry density samples (Figure 8c), where water menisci in macropores start to be identifiable. Water retention measurements (in particular, independence of water content on compaction level, Figure 3a) were consistent with these observations.

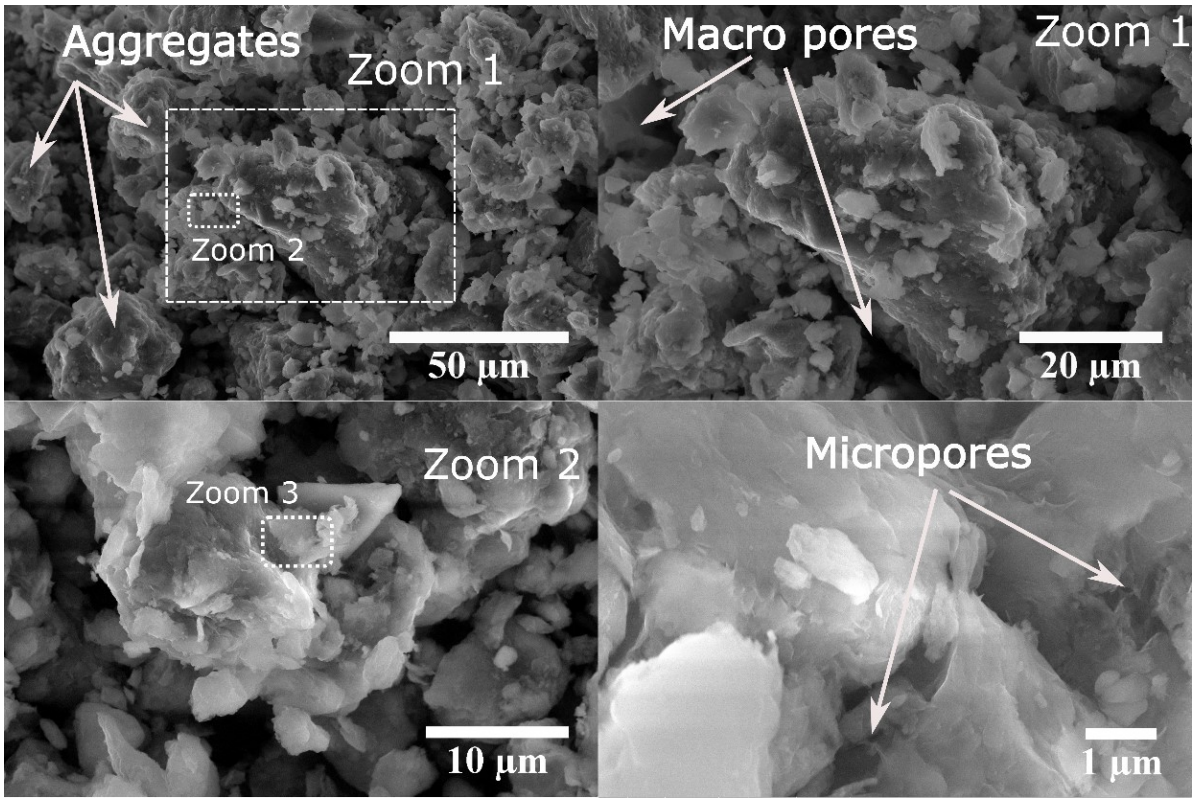


*Figure 6. ESEM micrographs of compacted bentonite with a dry density of 1.27 g/cm$^3$ at different magnifications (Sun et al., 2018a).*

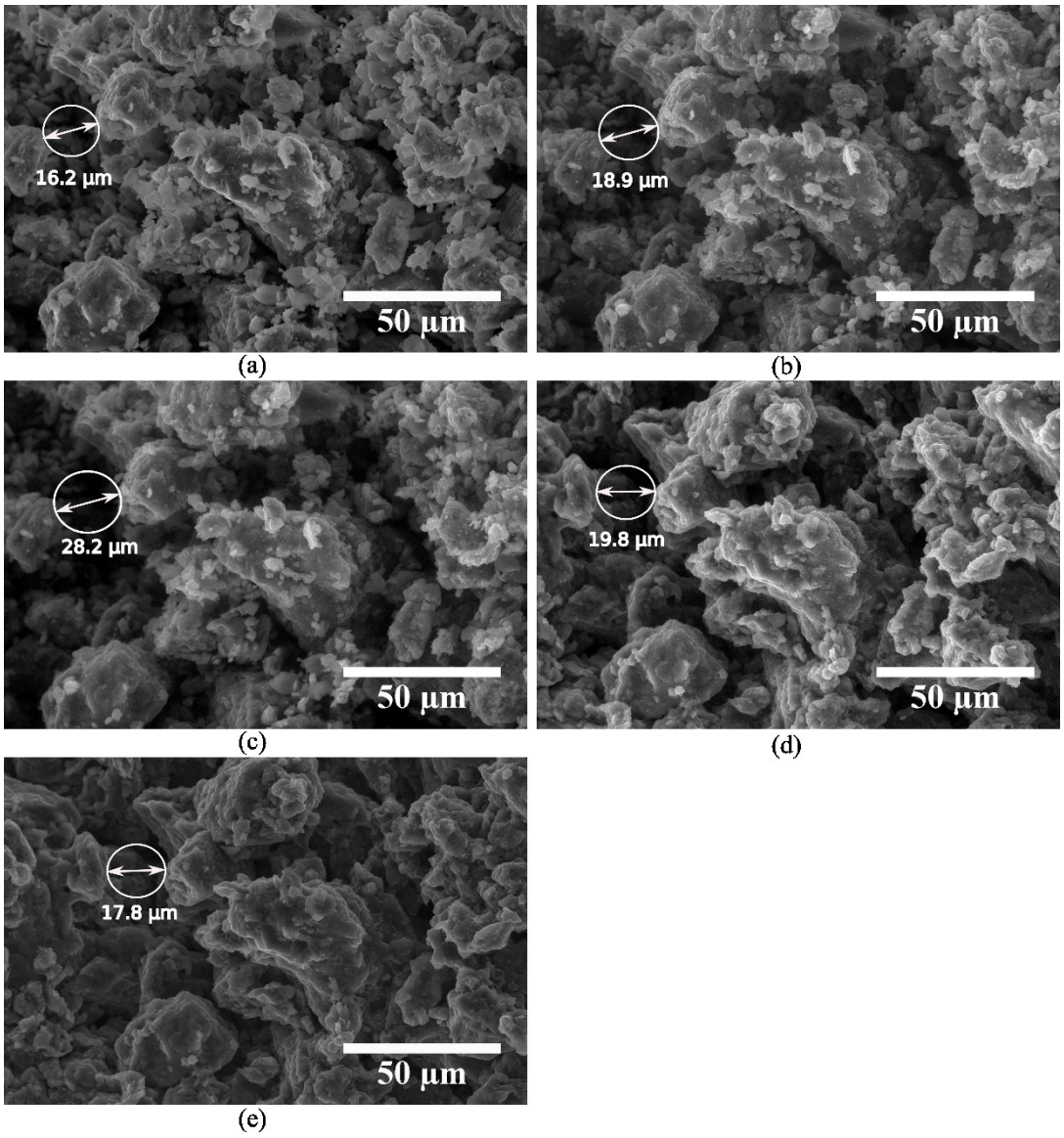


*Figure 7. Selected ESEM micrographs of compacted bentonite with a dry density of 1.27 g/cm$^3$ under the wetting–drying path: (a) 290.75 MPa; (b) 38.02 MPa; (c) 3.3 MPa; (d) 38.02 MPa; (e) 290.75 MPa (Sun et al., 2018a).*

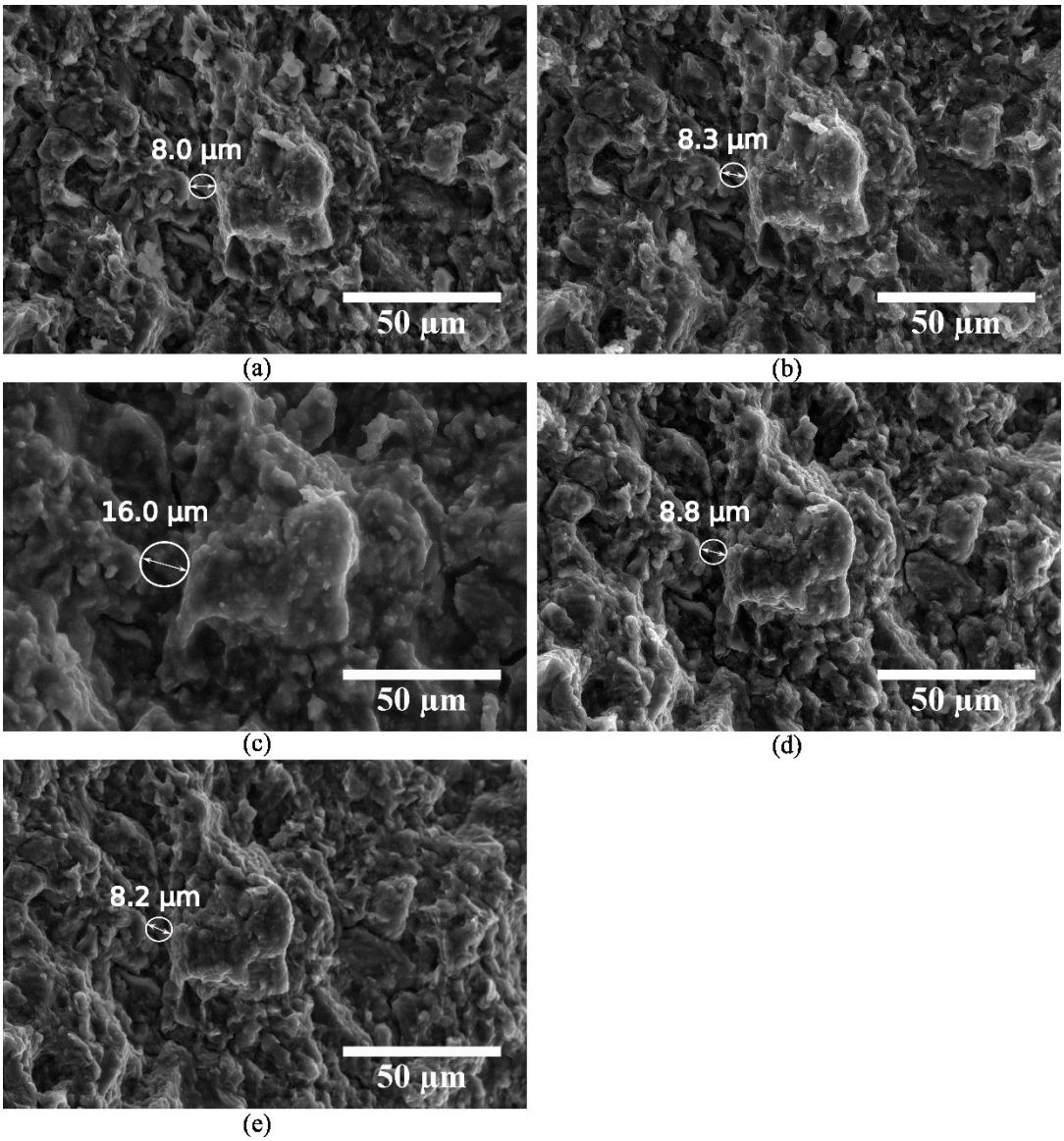


*Figure 8. Selected ESEM micrographs of compacted bentonite with a dry density of 1.90 g/cm$^3$ under the wetting–drying path: (a) 290.75 MPa; (b) 38.02 MPa; (c) 3.3 MPa; (d) 38.02 MPa; (e) 290.75 MPa (Sun et al., 2018a).*

### 4.2.3 Fractal characteristics of pores

Pore surface fractal dimension ($D_s$) was calculated based on Menger fractal dimension model and its calculation procedures were shown in equation (2) (Romero 1999). Thermal fractal dimension ($D_z$) was calculated based on thermal dynamic relation of the porous medium (Zhang and Li 1995) and its calculation procedures were shown from equation (3) to (6). The pore surface fractal dimension ($D_b$) was calculated based on box counting method from ESEM

images (Grau et al., 2006). The calculation of $D_s$ and $D_z$ were based on the MIP data, while the calculation of $D_b$ was based on the ESEM images.

$$\log[(dV_p/dV_{max})/d_p] \propto (D_s - 4)\log p \quad (2)$$

where p is the intrusion pressure (MPa), $V_p$ is the cumulative volume intruded for a given pressure p, $V_{max}$ is the total volume intruded for the maximum intrusion pressure and $D_s$ is the surface fractal dimension. The interval zones of self-similarity and the different types of pore structure can be obtained from the linear sections of $\log[(\frac{dV_p}{dV_{max}}/dp)$ versus log p, the slope of which yield the values of fractal dimension.

The calculation of $D_z$ is based on thermal dynamic relation of porous medium in the process of mercury intrusion porosimetry. It is considering the equilibrium of surface energy increased by mercury intrusion and work done by surroundings as shown in the following equations,

$$\ln(W_n) = \ln(Q_n) + C \quad (3)$$

$$\text{Let } Q_n = r_n^{2-D_z} V_n^{D_z/3} \quad (4)$$

$$W_n = \sum_{i=1}^{n} \overline{p_i}\Delta V \quad (5)$$

Substituting Equation (4) and (5) in to equation (3) leads to:

$$\ln(W_n/r_n^2) = D_z \ln\left(\frac{V_n^{\frac{1}{3}}}{r_n}\right) + C' \quad (6)$$

where *i* means *i*-th intrusion step, *n* means total intrusion number, $\overline{p_i}$ is the average intrusion pressure for ith intrusion, $\overline{p_i}\Delta V$ is the increased intrusion volume for *i*-th intrusion, *r* is the pore radius, C and C` are constants, $D_z$ is fractal dimension calculated from thermal dynamic relations, $W_n$ is the accumulated surface energy, $Q_n$ is a function of pore radius and pore volume.

The relation between fractal dimension and magnification for low and high dry density samples is shown in Figure 9. The results showed a decrease in $D_b$ with increasing magnification, which was followed by an increase at high magnifications (the increase is however indicated by few data points only). $D_b$ has a linear relationship with logarithm of magnification for both dry densities until the threshold value at magnification of 10 000 for lower dry density and 25 000 for higher dry density samples.

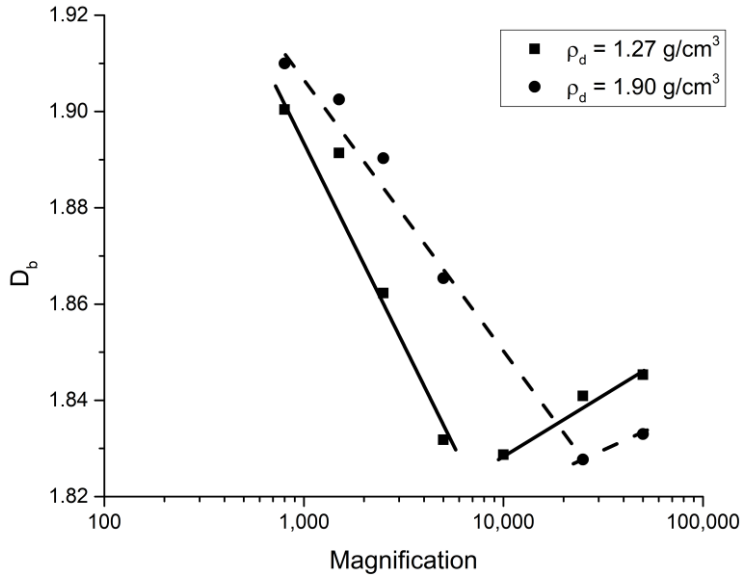


*Figure 9. Surface fractal dimension ($D_b$) versus magnification, low dry density of 1.27 g/cm$^3$ (a) and high dry density of 1.9 g/cm$^3$ (b) (Sun et al., 2019)*

The calculated $D_s$ value was dependent on the pore size range, the fractal dimension for both dry densities and all suctions were plotted in one graph shown in Figure 10. Both micropores and macropores can clearly be identified based on the fractal analysis. Inside the family of macro-pores, fine macropores and coarse macropores can be distinguished. Micropores were represented by parallel regression lines of all samples demonstrating similar values of surface fractal dimension $D_s$. It showed that this domain representing the pores inside the aggregates was compaction-insensitive. The size of the micro-pores domain was therefore not uniquely defined and depended on the value of suction. The macropores and micropores were defined based on the fractal analysis, which was consistent with the pore size distribution curves presented by Sun et al. (2019). Although different calculations were used which were based on different nature of methods in the evaluation, it can be summarized that the pores fractal dimension decreased slightly with decreasing suction ($D_b$ evaluated using wetting tests, $D_s$ on low density samples and $D_z$ for both dry densities). More details was presented in the attached paper 2 (Sun et al., 2019).

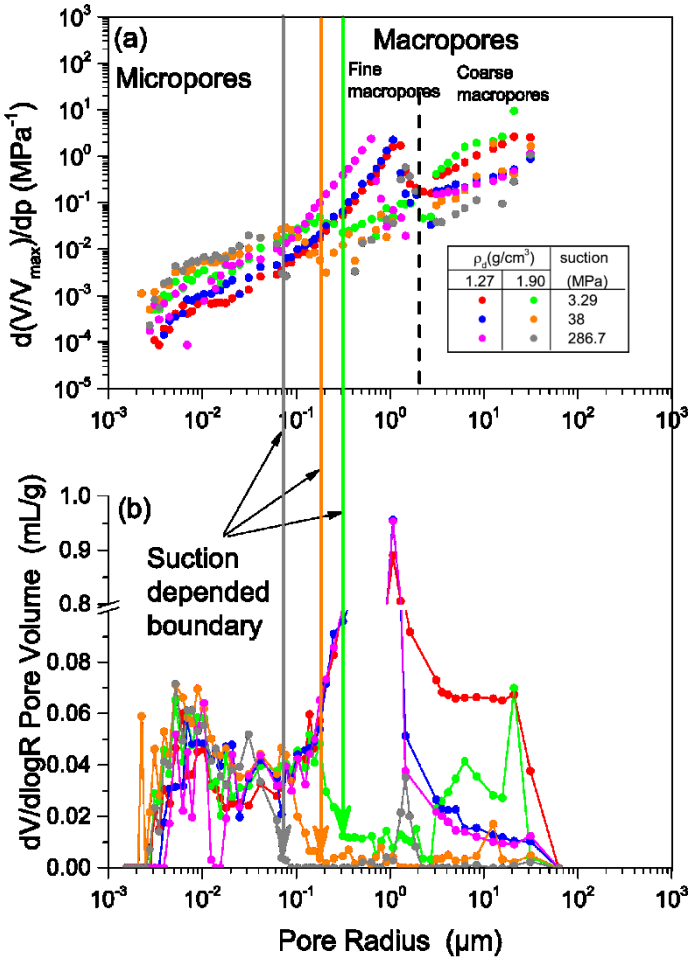


*Figure 10. Fractal dimension (a) and pore size distribution (b) with pore radius under each suction level for both dry densities (Sun et al., 2019)*

## 4.3 Mechanical behavior

In this chapter, the experiments on one-dimensional swelling performed on compacted bentonite with various initial dry densities, namely 1.25 g/cm$^3$, 1.80 g/cm$^3$, and 1.95 g/cm$^3$ are described. The tests were performed to explore the influence of vertical stress and initial dry density on swelling strain. The values of swelling pressure determined by swell-consolidation method and constant volume test were compared. The obtained results presented in subsection 4.3.1 were presented and published in UNSAT2018 conference proceedings (Sun et al., 2018c). A proposed swelling pressure model based on the diffuse double layer (DDL) theory was developed by the author by consideration of the void ratio. The model and its predictions presented in subsection 4.3.2 were published in Geomechanics and Engineering journal (Sun,

2018). Further, the developed model was used to predict the swelling pressure of the compacted Czech bentonite.

### 4.3.1 Swelling behavior

The vertical load and measured maximum swelling strain are depicted in Figure 11(a). The decrease of swelling strain with increasing vertical stress shows a linear trend in semi-logarithmic scale and moves towards higher vertical loads with increasing dry density. The final void ratio and vertical load curves are shown in Figure 11.(b). It can be seen that the final void ratio decreases with increasing vertical load linearly in a semi-logarithmic scale at high vertical load range. The e-log p curves are independent of the initial dry density.

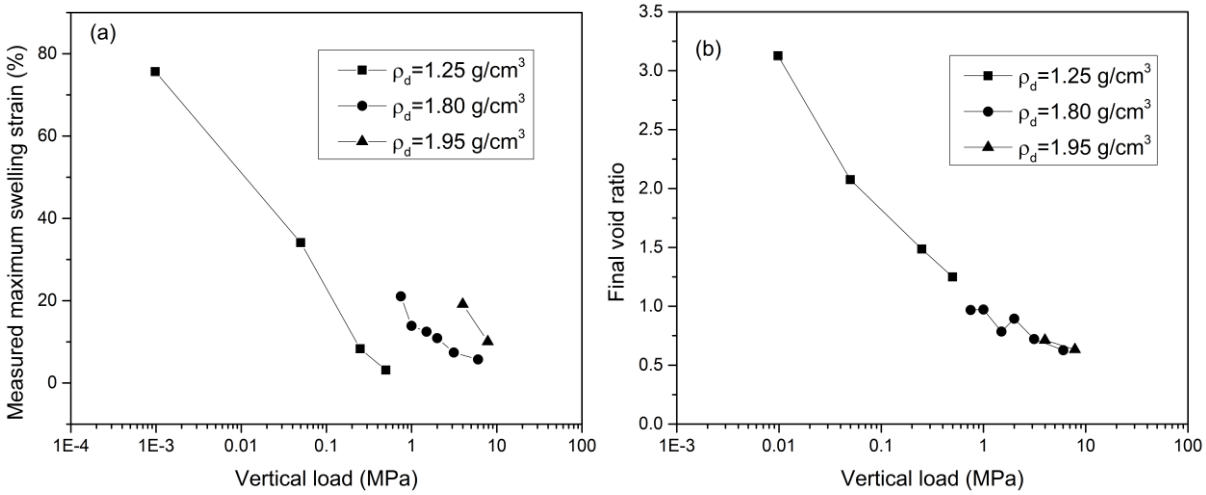


*Figure 11. Maximum swelling strain (a) and final void ratio (b) vs. vertical load*

Figure 12 shows the loading-unloading path and constant volume tests of two kinds of compacted bentonites plotted in vertical/swelling pressure vs. dry density at saturation. The results of Czech B75 bentonite (Hausmannova and Vasicek, 2014) (Figure 12b) indicate that the swelling pressure measured by constant volume test was lower than the swelling pressure (i.e., applied pressure) determined by "swell-consolidation" method. The same results were presented by Baille et al. (2010) on Bavaria bentonite. The difference between the applied pressure and swelling pressure increased with the increase of dry density for both bentonites. The differences was strongly dependent on the stress path (OC&OAB in Figure 2) and the initial dry density, which affected the fabric and macro-micro structure of the clay (Gens and Alonso, 1992). Different $K_0$ values can also be a reason for different vertical swelling pressures.

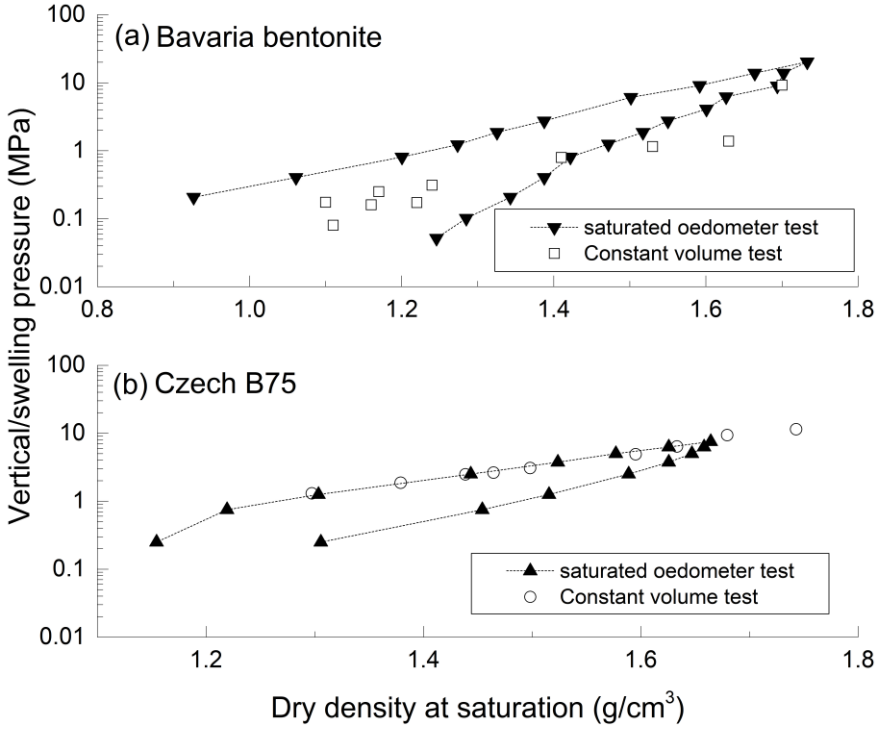


*Figure 12. Comparison of vertical/swelling pressure vs dry density at saturation (saturated oedometer test & constant volume test) of (a) Bavaria bentonite (Baille et al., 2010), (b) Czech B75 (Hausmannova and Vasicek,2014).*

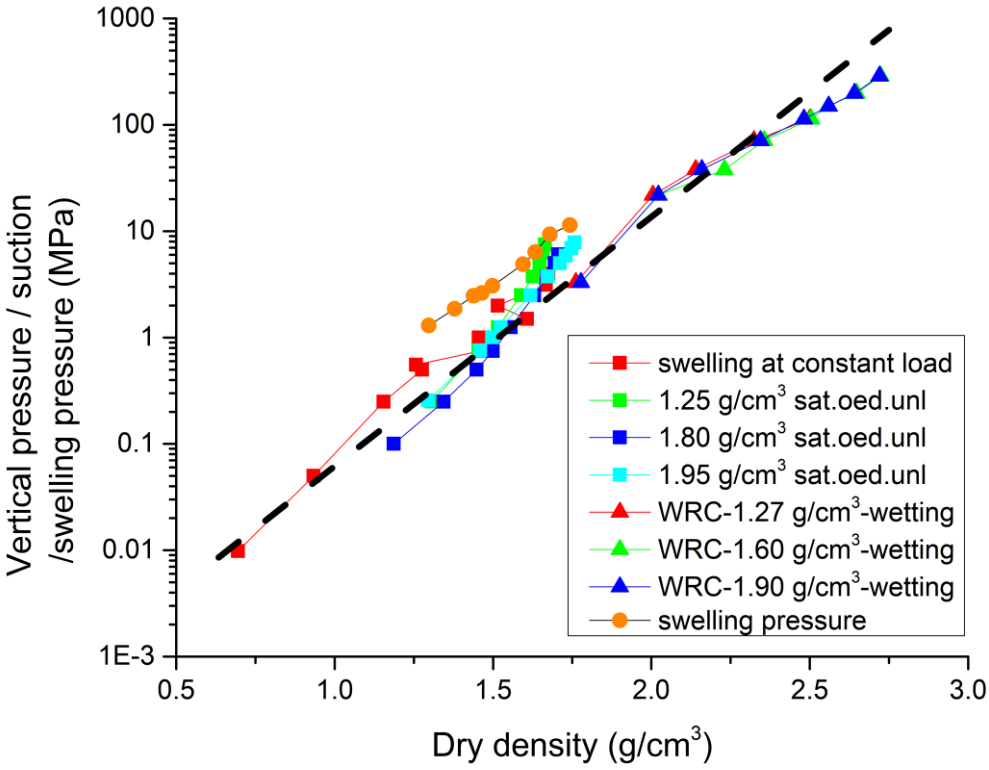


*Figure 13. Swelling pressure (Hausmannova and Vasicek, 2014), oedometer unloading pressure, oedometer constant pressure and suction versus dry density*

In order to investigate the evolution of wetting-induced swelling pressure by changing of dry density (void ratio), several experiments were performed, which included the unconfined water retention curves, swelling pressure tests, swelling under constant load tests and oedometer unloading test. Three different initial dry densities of 1.25, 1.80 and 1.95 g/cm$^3$ were used for the oedometer constant load tests and oedometer unloading tests, another three dry densities of 1.27, 1.60 and 1.90 g/cm$^3$ were used for the water retention tests. The initial dry density of 1.2-1.80 g/cm$^3$ was used for the swelling pressure tests. Here the dry density referred to the dry density of the aggregates, the method adopted for calculation was presented by Mašín and Khalili (2015). All the results are shown in Figure 13. A unique linear trend occurred between pressure and dry density, but swelling pressure tests gave higher pressures than other methods. This unique relationship showed that the bentonite deformation depends only on the effective stress, which is consistent with the Terzaghi's effective stress definition.

### 4.3.2 Swelling pressure model

The swelling pressure is the difference between the osmotic pressure in the central plane between two clay platelets and the osmotic pressure in the equilibrium solution (Bolt 1956). The osmotic pressure at the central plane between clay platelets can be calculated from Gouy-Chapman diffuse double layer theory which originally was presented by Bolt (1956) and Van Olphen (1963) and improved by Sridharan and Jayadeva (1982). The following equations are used to establish the theoretical relationship between swelling pressure and dry density:

$$e = G\gamma_w Sd * 10^6 \tag{7}$$

$$\gamma_d = \frac{G\gamma_w}{1+e} \tag{8}$$

$$\int_z^u \frac{1}{\sqrt{(2\cosh y - 2\cosh u)}} dy = \int_0^d d\zeta = -Kd \tag{9}$$

$$-\left(\frac{dy}{d\zeta}\right)_{x=0} = \sqrt{(\cosh z - 2\cosh u)} = \left(\frac{B}{S}\right)\sqrt{\frac{1}{2\varepsilon_0 D n_0 kT}} \tag{10}$$

$$\mathrm{p} = 2n_0 kT(\cosh u - 1) \tag{11}$$

$$\mathrm{K} = \left(\frac{2n_0 e'^2 v^2}{D_w kT\varepsilon_0}\right)^{\frac{1}{2}} \tag{12}$$

Where e is the void ratio of compacted bentonite, G is the specific gravity, $\gamma_w$ is the density of water, $\gamma_d$ is the dry density, S is the specific surface area (m$^2$/g), d is the half of the distance of clay platelets (m), u is the nondimensional midplane potential, y is the nondimensional potential at a distance x from the clay surface, z is the nondimensional potential function at the surface

(x = 0), ζ is the distance function (ζ = Kx), B is the base cation exchange capacity (meq/100g), $\varepsilon_0$ is the permittivity of vacuum (8.8542×10-23 $C^2J^{-1}m^{-1}$), $D_w$ is the dielectric constant of bulk fluid (80.4 for water), $n_0$ is the ionic concentration of the bulk fluid in ions/$m^3$, k is the Boltzmann's constant ($1.38\times10^{-23}$ J/K), K is the diffuse double layer parameter (1/m), T is the absolute temperature in Kelvin, p is the swelling pressure (Pa), e` is the elementary electric charge ($1.602\times10^{-23}$ C), v is the weighted averaged of valency of exchangeable cations (Tripathy et al., 2004).

Sridharan and Jayadeva (1982) summarized the relationships between u and log(Kd) for different values of $(dy/d\zeta)_{x=0}$. A linear relationship between u and log(Kd) was suggested to compute u value by knowing Kd. The swelling pressure can be predicted by relating the value of u obtained from equation (11) and Kd for any given properties of bentonite and the known bulk fluid properties (Sridharan and Jayadeva 1982, Tripathy et al, 2004). For a range of assumed swelling pressure, the value of u can be obtained from equation (11) and the value of z can be calculated from equation (10). The value of Kd also can be calculated from equation (9) by knowing u and z. The value of K can be determined by equation (12), so the value of d can be obtained from equation (9). Knowing d, equation (7) can be used to calculate e. The dry density can be calculated from equation (8). The integration of equation (9) is evaluated numerically using the "quad" MATLAB method. Thus the theoretical relationship between swelling pressure and dry density can be obtained.

Severval types of compacted sodium and calcium bentonites were used in this section and their references are listed below.

1) MX80 compacted bentonite: Bucher and Müller-Vonmoos (1989)
2) Kunigel-V1 compacted bentonite: Japan Nuclear Cycle Development Institute (1999)
3) Voclay compacted bentonite: Komine (2004)
4) Neokunibond compacted bentonite: Komine (2004)
5) GMZ compacted bentonite: Schanz and Al-Badran (2014)
6) FoCa compacted bentonite: Imbert and Villar (2006)
7) FEBEX compacted bentonite: ENRESA (2000)
8) Montigel compacted bentonite: Bucher and Müller-Vonmoos (1989)

9) Bentonite S-2 compacted bentonite: ENRESA (2000)

10) Bavaria bentonite: Schanz and Tripathy (2009)

Considering the difference of the preserved cations in different bentonites, the mineral components and the difference between theoretical and measured swelling pressure, two representative bentonites were chosen. Here, the MX80 and FoCa bentonite contained the highest sodium and calcium content respectively, also they have the average montmorillonite content among Na-bentonite and Ca-bentonite. Therefore, MX80 and FoCa bentonite can be regarded as the representative of Na-bentonites and Ca-bentonites in this research, respectively. The results show that there exists a large difference between theoretical and actual experimental data. From the expression of equation (11), an attempt was made to revise the relationship between u and log(Kd). An idea came out that the difference of experimental and theoretical non-dimensional mid-plane potential, Δu, should follow the same trend with dry density. The growth form of hyperbolic function cosh(u) and exponential function followed the same style. Based on this, it was assumed that Δu has an exponential increase with dry density. Here, void ratio was chosen instead of dry density considering the non-dimensional form of void ratio. Based on the experimental information of MX80 and FoCa bentonite, the relationship between Δu and e was established for Na-bentonites and Ca-bentonites. The following equations (13) & (14) were suggested for Na-bentonites, (15) & (16) for Ca-bentonites,

$$p=2n_0kT[\cosh(u_{theory}+\Delta u_{MX80})-1] \quad (13)$$

$$p=2n_0kT[\cosh((-3.462\log(Kd)+3.292)-1.729\ln(e+0.203))-1] \quad (14)$$

$$p=2n_0kT[\cosh(u_{theory}+\Delta u_{FoCa})-1] \quad (15)$$

$$p=2n_0kT[\cosh((-3.957\log(Kd)+2.869)-5.158\ln(e+0.153))-1] \quad (16)$$

The swelling pressure data of the experimental and predicted values of all the bentonites were drawn in abscissa and ordinate respectively as shown in Figure 14. The nearer the points closed to the 1:1 line (dash line), the more accurate the model predicted. It can be seen that the proposed equations have a little defect to predict the swelling pressure (0.3~0.9 MPa) of Kunigel-V1, but it was much better than the theoretical diffuse double layer theory prediction. It also can be observed that part of the Bavaria bentonite data (0.06~0.3MPa) was far from the dash line, but this didn't mean that the model can't work well on Bavaria bentonite. Because of the very small range, even a very tiny difference can show a big amplification in the logarithmic coordinates. Therefore, the agreement between experimental data and predicted swelling

pressure showed that the proposed equation (13) and equation (15) were effective in the prediction of swelling pressure for compacted Na-bentonites and Ca-bentonites.

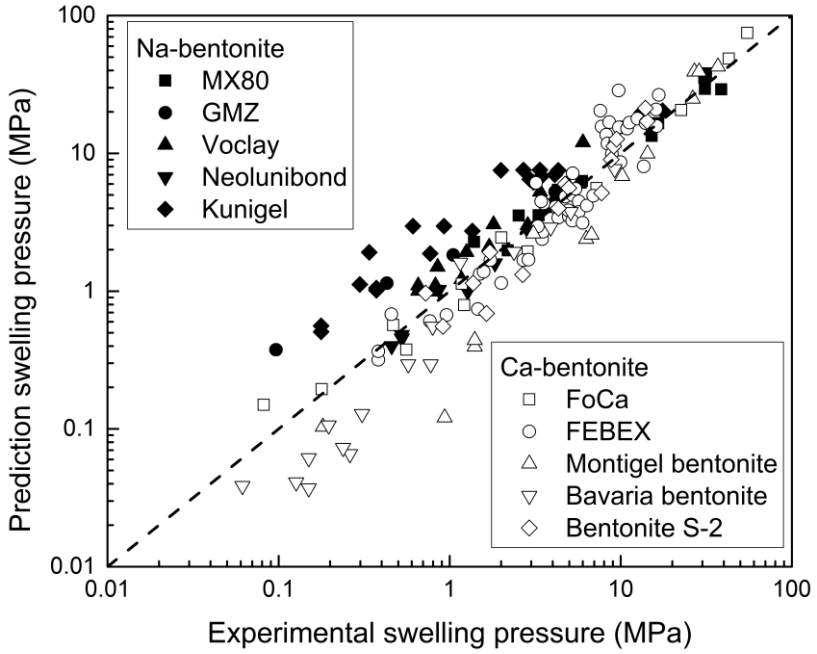


*Figure 14. Experimental swelling pressure versus prediction swelling pressure for all the compacted bentonite*

### 4.3.3 Model validation by Czech bentonite

The swelling pressure of Czech bentonite was used to further to check the developed model. There were two types of bentonite namely Sab65 bentonite which was sodium bentonite, another was the B75 bentonite, which is a calcium-magnesium bentonite. The experimental data were obtained from Hausmannova and Vasicek (2014). The parameters used to calculate the swelling pressures are shown in Table 6. Figure 15 showes the experimental data compared with the theoretical value and developed model predictions. It can be seen that the proposed model prediction is much better than the theoretical DDL values. However, the theoretical DDL values were predicted well when the dry density was lower than 1.55 g/cm$^3$, this phenomena was presented by Tripathy et al. (2004), Schanz and Tripathy (2009) and Sun (2018).

It is necessary to point out that the swelling pressure is not only determined by diffuse double layers, but also depends on other factors such as the hydration energy of the cations, the electrostatic forces between cations and anions, the van der Waals force, etc. All these factors

influence the swelling pressure of compacted bentonite, the developed diffuse double layer model should be improved by considering these factors in the future.

*Table 6. Parameters of Sab65 and B75*

| | $n_0$ (mol/L) | B (meq/100g) | Crystallographic S ($m^2/g$) | v |
|---|---|---|---|---|
| Sab 65 | 0.0001 | 117.19 | 713[a] | 1.1 |
| B75 | 0.0001 | 80.47 | 730[a] | 1.78 |

a- data from Fernandez A.M. (2015)

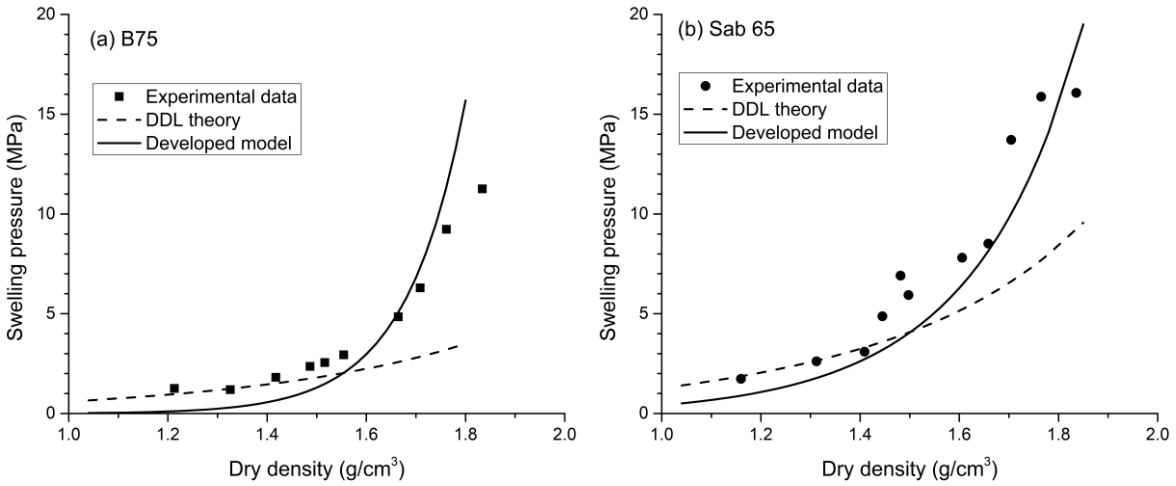


*Figure 15. Theoretical DDL prediction, experimental and developed model for swelling pressure of Czech bentonite (a) B75 and (b) Sab65*

# 5. Conclusions

In the thesis, I presented experimental and theoretical works on the water retention properties, microstructure characteristics and mechanical behavior of compacted Czech bentonite. The following conclusions can be drawn:

Water retention properties:

1) No variations of retention curves (water content vs. suction) with initial dry density was observed at 20°C and the same result was confirmed at higher temperatures. This conclusion is due to the fact that suctions adopted are quite high, where no water is between aggregates. The water retention capacity of compacted bentonite decreased with increasing temperature for all the dry densities. This trend is more obvious for drying paths. For wetting path and suctions over 100 MPa, no obvious change of the retention capacity with temperature was observed.

Microstructural analysis:

2) Apart from the inter-lamellar pores, which were not accessible to the adopted observation methods, two main pore families (macropores and micropores) could be identified. Their transition pore size was suction dependent (0.07 to 0.3 μm for suctions varying between 286.7 and 3.29 MPa). The micropores were practically insensitive to compaction and only the largest micropores were sensitive to suction. The smaller macropores were sensitive to compaction only, whereas the larger macropores were sensitive to both compaction and suction.

3) Two pore size domains (macropores and micropores) were defined based on the fractal analysis of MIP data. The macropores can be subdivided to fine macropores and coarse macropores. The zones influenced by suction and different compaction energy were identified. An estimation of pore geometry of different size domains can be made based on the value of fractal dimension $D_s$. Pore size domains determined from fractal analysis correlates with size domains obtained by visual evaluation of MIP distribution curves. The fractal analysis of MIP data thus proved to be a useful tool, which complements the information obtained from MIP distribution curves.

4) The fractal analysis using the box counting method on ESEM images proved high fractal characteristics of bentonite pore system. The fractal dimension decreases with increasing magnification due to more smooth and regular structures observed under high magnifications. However, the fractal dimension increases again when approaching extremely high magnifications. The effect of freeze-drying and oven-drying was investigated, showing a higher fractal dimension of oven dried samples. This indicates a certain change of the pore structure of the samples exposed to oven drying.

Mechanical behavior:

5) The swelling-consolidation method gives a higher swelling pressure than constant volume method because of the crystalline expansion and osmotic expansion. The swelling pressure determined by constant volume method and dry density at saturation shows a good linear relationship in semi-logarithmic coordinates. This unique relationship showed that the bentonite deformation depends on the effective stress only, which is consistent with the Terzaghi's effective stress definition.

6) The newly proposed equations based on DDL theory were developed by consideration the variablity of void ratio. The swelling pressures calculated by proposed equations indicated a good agreement with the experimental swelling pressures. Moreover, this proposed model worked well for Czech Sab65 bentonite, while it was less accurate on Czech B75 bentonite at lower dry density range.

# 6. References

Alonso, E. E., Pereira, J. M., Vaunat, J. & Olivella, S. (2010). A microstructurally based effective stress for unsaturated soils. *Géotechnique* 60, No. 12, 913–925, https://doi.org/10.1680/geot. 8.P.002.

Alonso, E. E., Vaunat, J. & Gens, A. (1999). Modelling the mechanical behaviour of expansive clays. *Engng Geol*. 54, No. 1–2, 173–183.

ASTM D2435 / D2435M: Standard Test Methods for One-Dimensional Consolidation Properties of Soils Using Incremental Loading.

Baille, W., Tripathy, S. and Schanz, T., 2010. Swelling pressures and one-dimensional compressibility behavior of bentonite at large pressures. *Appl. Clay Sci*. 48, 324–333.

Basma, A., Al-Homoud, A. S. and Husein.A., 1995. Laboratory assessment of swelling pressure of expansive soils. *Applied Clay Science*, 9 (5), pp. 355–368.

Bolt, G.H. (1956). Physico-chemical analysis of the compressibility of pure clays. *Géotechnique*, 6(2): 86–93. doi: 10.1680/geot.1956.6.2.86.

Bucher, F and Müller-Vonmoos, M. (1989). Bentonite as a containment barrier for the disposal of highly radioactive waste. *Applied Clay Science*, 4(2): 157–177. doi: 10.1016/0169-1317(89)90006-9

Chapman, D.L. (1913). A contribution to the theory of electro-capillarity. *Philosophical Magazine*, 25: 475–481. doi: 10.1080/14786440408634187.

Chen, F.H., 1988. Foundations on expansive soils, 2nd ed. Elsevier Science Publishing Co., Inc., New York.

Cui ZD, Zhao LZ, Yuan L (2016) Microstructures of consolidated Kaolin clay at different depths in centrifuge model tests. *Carbonates and Evaporites*, 31(1), 47-60.

Delage, P., Howat, M. D. & Cui, Y. J. (1998). The relationship between suction and swelling properties in a heavily compacted unsaturated clay. *Engng Geol*. 50, No. 1–2, 31–48.

Dieudonne, A. C., Della Vecchia, G. & Charlier, R. (2017). Water retention model for compacted bentonites. *Can. Geotech. J*. 54, No. 7, 915–925.

ENRESA. (2000). FEBEX project — full scale engineered barriers experiments for a deep geological respiratory for high level radioactive waste in crystalline host rock. Final report, Publicación téechnica 1/2000, Empresa Nacional de Residuos Radiactivos SA (ENRESA), Madrid, Spain.

## 6. References


Farulla CA, Jommi C (2005, May) Suction controlled wetting-drying cycles on a compacted scaly clay. In *Proceedings of international conference on problematic soils*(Vol. 25, p. 27).

Fernandez A.M. (2013), Influence of the physico-chemical and crystallographic properties of clay minerals on erosion processes, presentation.

Flavio SA, Stefan L, Gregor PE (1998) Quantitative characterization of carbonate pore systems by digital image analysis. *AAPG Bulletin* 82 (10), 1815–1836.

Gens, A. & Alonso, E. E. (1992). A framework for the behaviour of unsaturated clays. *Can. Geotech. J.* 29, No. 6, 1013–1032.

Gouy, G. (1910). Electric charge on the surface of an electrolyte. *Journal of Physics*, 4(9): 457.

Grau J, Méndez V, Tarquis AM, Diaz MC, Saa A (2006) Comparison of gliding box and box-counting methods in soil image analysis. *Geoderma*, 134(3-4), 349-359.

Hansen JP, Skjeltorp AT (1988) Fractal pore space and rock permeability implications. *Physical review B*, *38*(4), 2635.

Hattab, M., Hammad, T., Fleureau, J. M. & Hicher, P. Y. (2013). Behaviour of a sensitive marine sediment: microstructural investigation. *Géotechnique* 63, No. 1, 71–84, https://doi.org/ 10.1680/geot.10.P.104.

Hausmannova, L. & Vasicek, R. (2014). Measuring hydraulic conductivity and swelling pressure under high hydraulic gradients. Geological Society, London, Special Publications 400, 293–301, https://doi.org/10.1144/SP400.36.

Haynes, W.M., 2014. CRC handbook of chemistry and physics. CRC press.

Hyslip JP, Vallejo LE (1997) Fractal analysis of the roughness and size distribution of granular materials. *Engineering geology*, *48*(3-4), 231-244.

Imbert, C., and M. V. Villar (2006), Hydro-mechanical response of a bentonite pellets/powder mixture upon infiltration, *Appl. Clay Sci*., 32, 197– 209, doi: 10.1016/j.clay.2006.01.005.

Japan Nuclear Cycle Development Institute. (1999). H12: project to establish the scientific and technical basis for HLW disposal in Japan: supporting report 2 (respiratory design and engineering Technology). Japan Nuclear Cycle Development Institute, Tokyo.

Juang, C. H. & Holtz, R. D. (1986). A probabilistic permeability model and the pore size density function. *Int. J. Numer. Analyt. Methods Geomech*. 10, No. 5, 543–553.

Komine, H., (2004). Simplified evaluation for swelling characteristics of bentonites, *Engineering geology*, 71(3-4): 265-279. doi: 10.1016/S0013-7952(03)00140-6.

Komine, H., and Ogata, N. (1996). Prediction for swelling characteristics of compacted bentonite. *Canadian Geotechnical Journal*, 33: 11–22. doi: 10.1139/t96-021.

Liu X, Nie B (2016) Fractal characteristics of coal samples utilizing image analysis and gas adsorption. *Fuel*, *182*, 314-322.

Mahamud M, López Ó, Pis JJ, Pajares JA (2003) Textural characterization of coals using fractal analysis. *Fuel Processing Technology*, *81*(2), 127-142.

Mašín D, Khalili N. (2016). Swelling phenomena and effective stress in compacted expansive clays. *Canadian Geotechnical Journal* 53(1): 134-147.

Monroy, R., Zdravkovic, L. & Ridley, A. (2010). Evolution of microstructure in compacted London Clay during wetting and loading. *Géotechnique* 60, No. 2, 105–119, https://doi.org/10.1680/geot.8.P.125.

Nelson, J. D. et al., 2015. Foundation Engineering for Expansive Soils, ISBN: 978-0-470-58152-0.

OIML (The International Organization of Legal Metrology) (1996). The scale of relative humidity (RH) of air certified against saturated salt solutions. Paris, France: OIMLR 121.

Přikryl, R. & Weishauptová, Z. (2010). Hierarchical porosity of bentonite-based buffer and its modification due to increased temperature and hydration. *Appl. Clay Sci.* 47, No. 1–2, 163–170.

Romero, E. & Vaunat, J. (2000). Retention curves of deformable clays. In Experimental evidence and theoretical approaches in unsaturated soils. Proceedings of an international workshop on unsaturated soils (eds A. Tarantino and C. Mancuso), pp. 91–106. Rotterdam, the Netherlands: A.A. Balkema.

Romero, E. (1999). Characterisation and thermo-hydro-mechanical behaviour of unsaturated Boom-clay: an experimental study. PhD thesis, Universitat Politecnica de Catalunya, Barcelona, Spain.

Romero, E., Della Vecchia, G. & Jommi, C. (2011). An insight into the water retention properties of compacted clayey soils. *Géotechnique* 61, No. 4, 313–328, https://doi.org/10.1680/geot. 2011.61.4.313.

Romero E, Simms PH (2008) Microstructure investigation in unsaturated soils: A review with special attention to contribution of mercury intrusion porosimetry and environmental scanning electron microscopy. Geotechnical and Geological Engineering 26, 705–727

Schanz. T and Tripathy. S (2009). Swelling pressure of a divalent-rich bentonite: diffuse double-layer theory revisited, *Water Resources Research*, 45 (2), p. W00C12, doi: 10.1029/2007WR006495

Schanz.T and Al-Badran.Y. (2014) Swelling pressure characteristics of compacted Chinese Gaomiaozi bentonite GMZ01, *Soils Found*., 54 (4), pp. 748–759, doi: 10.1016/j.sandf.2014.06.026.

Seiphoori, A., Ferrari, A. & Laloui, L. (2014). Water retention behaviour and microstructural evolution of MX-80 bentonite during wetting and drying cycles. *Géotechnique* 64, No. 9, 721–734, https://doi.org/10.1680/geot.14.P.017.

Sridharan, A., and Jayadeva, M.S. (1982). Double layer theory and compressibility of clays. *Géotechnique*, 32(2): 133–144. doi: 10.1680/geot.1982.32.2.133.

Stastka, J. & Smutek, J. (2015). Experimental works with bentonite pellets at the CEG. Proceedings of the LUCOEX conference and workshop – full-scale demonstration tests in technology development of repositories for disposal of radioactive waste, Oskarshamn, Sweden, pp. 179–184.

Sun, H., Mašín, D., & Boháč, J. (2017). Experimental characterization of retention properties and microstructure of the Czech bentonite B75. In Proceedings of the 19th International Conference on Soil Mechanics and Geotechnical Engineering, Seoul (pp. 1249-1252).

Sun, H., Mašín, D., Najser, J., Neděla, V., & Navrátilová, E. (2018a). Bentonite microstructure and saturation evolution in wetting–drying cycles evaluated using ESEM, MIP and WRC measurements. *Géotechnique*, 1-14.

Sun, H., Mašín, D., & Najser, J. (2018b). Thermal Water Retention Characteristics of Compacted Bentonite. In GeoShanghai International Conference (pp. 71-78). Springer, Singapore.

Sun, H. (2018). A new method to predict swelling pressure of compacted bentonites based on diffuse double layer theory. *Geomechanics and Engineering*, 16(1), 71-83.

Sun, H., Mašín, D. Najser, J., Neděla, V., & Navrátilová, E. (2019), Fractal characteristics of pore structure of compacted bentonite studied by ESEM and MIP methods, *Acta Geotechnica* (Accepted).

Tang, A. M., and Cui, Y. J., 2005. Controlling suction by the vapour equilibrium technique at different temperatures and its application in determining the water retention properties of MX80 clay. *Canadian Geotechnical Journal*, 42(1), 287-296.

Tripathy, S., A. Sridharan, and T. Schanz (2004), Swelling pressures of compacted bentonites from diffuse double layer theory, *Can. Geotech. J*., 41, 437–450, doi: 10.1139/t03-096.

Turcotte DL (2002) Fractals in petrology. *Lithos*, *65*(3-4), 261-271.

Vallejo LE (1996) Fractal analysis of the fabric changes in a consolidating clay. Engineering Geology, 43(4), 281-290

Van Olphen, H. (1963). An introduction to clay colloid chemistry: for clay technologists, geologists and soil scientists. Interscience, New York. doi: 10.1126/science.143.3610.1023-a.

Villar, M. V. (2007). Water retention of two natural compacted bentonites. *Clays and Clay Minerals*, 55(3), 311-322.

Villar, M. V., and A. Lloret. 2004. Influence of temperature on the hydro-mechanical behaviour of a compacted bentonite. *Applied Clay Science* 26, no. 1: 337-350.

Wang, Q., Cui, Y. J., Tang, A. M., Li, X. L. & Ye, W. M. (2014). Time - and density - dependent microstructure features of compacted bentonite. *Soils Found*. 54, No. 4, 657–666.

Wong PZ, Howard J (1986) Surface Roughening and the Fractal Nature of Rocks. *Physical Review Letters* 57, 637–642.

Zhang B, Li S (1995) Determination of the surface fractal dimension for porous media by mercury porosimetry. *Industrial & Engineering Chemistry Research*, 34(4), 1383-1386

# 7. Attached publictions

**Sun, H**., Mašín, D., Najser, J., Neděla, V., & Navrátilová, E. (2019). Bentonite microstructure and saturation evolution in wetting–drying cycles evaluated using ESEM, MIP and WRC measurements. *Géotechnique*, 69(8), pp. 713-726, doi: doi.org/10.1680/jgeot.17.P.253

**Sun, H**., Mašín, D., Najser, J., Neděla, V., & Navrátilová, E. (2019). Fractal characteristics of pore structure of compacted bentonite studied by ESEM and MIP methods. *Acta Geotechnica*, DOI: 10.1007/s11440-019-00857-z. (Accepted manuscript)

**Sun, H**. (2018). A new method to predict swelling pressure of compacted bentonites based on diffuse double layer theory. *Geomechanics and Engineering*, 16(1), 71–83. https://doi.org/10.12989/GAE.2018.16.1.071